CHEMISTRY OF MATERIALS

Article

pubs.acs.org/cm

Revealing the Intrinsic Li Mobility in the Li_2MnO_3 Lithium-Excess Material

Yongwoo Shin,[†] Hong Ding,[†] and Kristin A. Persson*[,†,‡]

[†]Environmental Energy Technologies Division, Lawrence Berkeley National Laboratory, Berkeley, California 94720, United States

[‡]Department of Materials Science and Engineering, University of California Berkeley, Berkeley, California 94704, United States

Supporting Information

ABSTRACT: One of the most promising avenues for future high energy Li-ion batteries originate from the family of Li-rich layered cathodes. However, while exhibiting excellent initial capacity, these materials also suffer from voltage fade, high impedance, and poor rate capability, particularly in the Mn-rich, high Li excess concentration regime. Though it is clear that the Li_2MnO_3 component contributes to the high capacity as well as the chemical and structural degradation of the material, the inherent ionic conductivity of the material has not been clarified. In this work, we investigate the delithiation mechanism, involving coherent Li migration from two layers by first-principles density functional theory. Surprisingly, and contrary to expectations from available experimental results, we find that the pristine material exhibits excellent Li mobility enabling facile Li extraction from both the transition metal layer and Li-layer. Generally, the Li-extractions are highly accelerated by di- and trivacancy clusters, which stabilize the saddle point tetrahedral sites. Hence, we deduce that the observed inferior rate behavior of this class of Li cathode materials is not due to intrinsic poor bulk ionic mobility, but more likely due to surface-passivation, structural deterioration, and/or particle−particle electrode-level transport limitations.

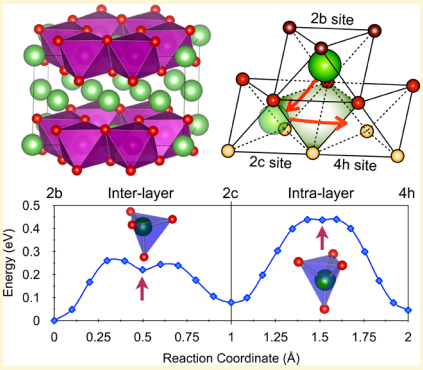

INTRODUCTION

Understanding the limitations in ionic mobility is highly important for many technologies, enabling materials optimization in such diverse areas as high-rate energy storage, solid state electrolytes, and ion-selective membranes. However, particularly in composite devices, identifying and deconvoluting the ion transport can be very challenging, as most techniques capture only the most rate limiting step, which can be determined on the composite particle-level, grain boundary/surface-level, and/or bulk level interactions. In this aspect, first-principles calculations can aid in identifying diffusion impediments by calculating the inherent response of the individual materials in their pristine state or under specific, controlled perturbations and/or environments. Such calculations have previously identified extremely high rate electrode materials such as $LiFePO_4$,[1,2] graphite,[3] as well as the superionic solid state electrolytes $Li_{10}GeP_2S_{12}$ (LGPS) derivatives.[4,5]

In this work we focus on the family of Li-excess Li-ion electrode materials,[6−8] which have attracted the interest of the community through the promise of significantly higher capacity compared to previously examined intercalation cathode materials. Unfortunately, inherently coupled with the higher capacity is observed structural degradation, increased impedance, poor rate behavior, and voltage fade.[9−13] Persistent efforts to overcome these obstacles have been undertaken; for instance, particle coatings to protect the material from irreversible reactions with the electrolyte,[14,15] doping schemes such as sodium(Na)-substitution ($Li_{2-x}Na_xMnO_3$) to enhance cycling stability,[16] and fluorine(F)-doping to increase the structural stability and cycling performance.[17,18]

While the Li-excess materials can be synthesized to display various microstructural and compositional features,[10,19] they share a common layered structure, comprised of a Li-layer and a combined Li/transition metal (TM) layer, where the excess is determined by the average amount of Li in the TM-layer. Whether exhibiting a composite structure or solid solution chemistry, the end member[20] on the spectrum in both cases is Li_2MnO_3 (see Figure 1a) which has the highest capacity but also exhibits the worst performance.[21,22] Hence, within the limits of a single-crystal model system (e.g., no grain boundaries or surfaces), the study of Li_2MnO_3 provides a "worst-case" representation of the family of layered Li-excess materials. Recently, there is growing evidence that the anomalously large capacity of Li_2MnO_3 originates from oxygen oxidation (as opposed to other suggested mechanisms such as proton exchange,[23−25] reversible oxygen loss,[24,26,27] etc.), which in turn renders the material unstable against Mn migration and subsequent structural deterioration and voltage fade.[13,24,28] Even low-rate, limited cycling of Li_2MnO_3 requires nanoscaling and higher temperatures.[21,28,29] Furthermore, galvanostatic intermittent titration measurements on composite Li_2MnO_3 electrodes indicate very slow Li diffusion.[30,31] Previous

Received: December 16, 2015
Revised: March 11, 2016

DOI: 10.1021/acs.chemmater.5b04862
Chem. Mater. XXXX, XXX, XXX−XXX

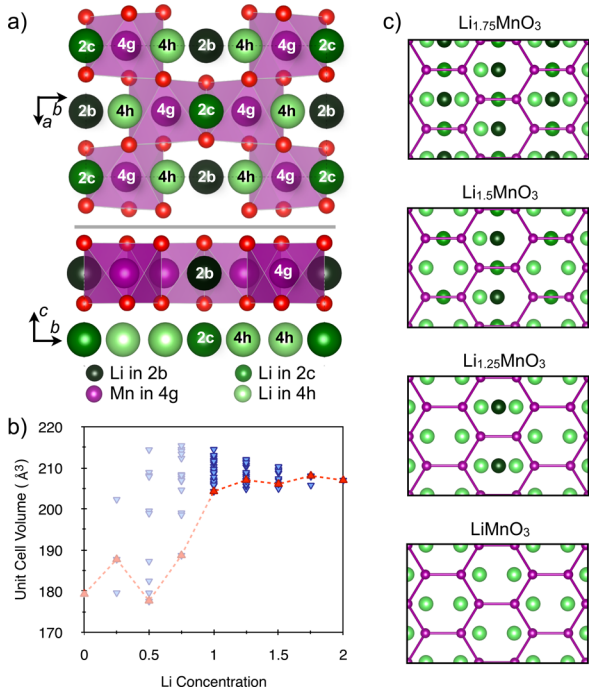

Figure 1. (a) Illustrations of the Li_2MnO_3 Li-excess structure. (b) Unit cell volume as a function of Li concentration for all Li-vacancy structures investigated in ref 23. For $1 < x < 2$, less than 3.6% (blue reverse triangle) change in unit cell volume is predicted, however, for $0 < x < 1$ significant structural deformations is expected (pale marks). The red triangles show the minimum energy structures for a given Li concentration. (c) Illustration of the delithiation process through the sequence of stable Li-vacancy configurations (red triangles in part b); $x = 1.75$; some Li are extracted from the 4h sites; $x = 1.5$; some Li are extracted from the 4h and 2b sites; $x = 1.25$; some Li are extracted from the 2b and 2c sites; finally, all 2b sites Li are extracted at $x = 1.0$.

computational work include a single-vacancy migration barrier[32] and defect energetics[13,33] in Li_2MnO_3. To improve upon our understanding and guide the optimization of this important class of intercalation materials, here we undertake a comprehensive study of the Li mobility, comprising the two layers, in pristine Li_2MnO_3 as a function of local cation-vacancy arrangements and possible Mn defects in the Li-layer.

RESULTS

As illustrated in Figure 1a, the layered, monoclinic Li_2MnO_3 structure consists of laminations of TM-layers and alternating Li-layers. The pristine structure exhibits two distinct octahedral sites in each layer, the 4g and 2b sites (TM-layer) and the 4h and 2c sites (Li-layer). In the pristine structure, Li diffusion in the Li-layer presumably occurs through Li-ion hops from its initial stable octahedral site to the nearest vacant octahedral site, through a tetrahedral site between the two adjacent octahedral sites. This is similar to the well-established Li diffusion patterns in other layered materials, e.g., $LiCoO_2$.[34] There are two types of tetrahedral sites in each layer, distinguished by their facet orientation to the crystallographically distinct octahedral sites. To label the migration patterns, we define the two distinct tetrahedral sites in the Li-layer as T^{Li}_{2b} and T^{Li}_{4g}, and similarly, the two tetrahedral sites in the TM-layer as T^{TM}_{2c} and T^{TM}_{4h}.

We focus our efforts on the high Li content region of Li_xMnO_3 ($1 < x < 2$) as deep delithiation is undesirable in this material due to its severe structural instability at lower Li contents.[21,24] Furthermore, a weak two-phase behavior or possibly solid-solution[31] is predicted in the $1 < x < 2$ Li concentration range, which is emphasized by the limited structural change as a function of Li content, e.g., less than 3.6% (Figure 1b) change in volume, indicating a smooth, Vegard's law dependence. This allows us to study the Li mobility in this concentration range as an approximate smooth function of the vacancy concentration.[35]

Previous theoretical[24,36] as well as experimental[37] work have shown that Li-ions can be extracted from both the TM-layer and the Li-layer, as illustrated in Figure 1c. From thermodynamic considerations, we recently[24] found that the delithiation process between $1 < x < 2$ favors the following steps: (i) some Li-ions are extracted from the 4h sites (Li-layer), (ii) some Li-ions are extracted from the 2b sites (TM-layer), (iii) all Li-ions in the 2c sites (Li-layer) are extracted, while some Li-ions in the 2c sites move into the vacant 4h sites, and finally (at $x = 1$) (vi) all Li-ions in the 2b sites (TM-layer) are extracted. In the following, we use this information as a starting point to systematically map out and investigate the Li mobility as a function of the local cation landscape and vacancy configuration in the two layers.

Intralayer Li-Ion Migration. In this section we present the results for Li migration *within* the Li-layer. As previously noted, the extraction mechanism of mobile Li-ions in layered materials is usually strongly related to the stability of the intermediate, "activated" tetrahedral site which connect the original and the final Li octahedral site.[34] However, for the Li excess materials where Li is present in both the Li-layer as well as the TM-layer, there exist more variations in the local cation landscape surrounding a mobile Li than in regular stoichiometric layered materials. Hence, in the following we perform a systematic exploration of the Li activation barriers, as a function of local cation topology.

Figure 3a shows a schematic structure of the Li-layer, where green and purple triangles represent the activated T^{Li}_{2b} and T^{Li}_{4g} sites, respectively. There exist four symmetry-distinguishable migration paths with respect to their migrating directions, which are (i) 4h−T^{Li}_{4g}−4h, (ii) 4h−T^{Li}_{2b}−4h, (iii) 4h−T^{Li}_{4g}−2c, and (iv) 4h−T^{Li}_{2b}−2c. From Figure 2 we note that path (i) and

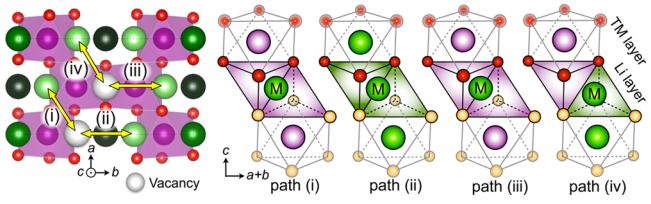

Figure 2. Illustration of the four symmetry-distinguishable migration paths (i), (ii), (iii), and (iv) as indicated by their local cation environment.

(iii) face-share with octahedral Mn sites in the layers both above and below, while path (ii) face-shares only with the octahedral Li sites in the adjacent layers. Path (iv) face-shares with the octahedral Mn site on one side and the octahedral Li site on the other. First, we examine the single-vacancy Li migration paths corresponding both to the oxygen dumbbell[38] (or oxygen edge[24]), where the Li moves straight through a dumbbell of oxygen, as well as the tetrahedral path, where the Li slightly deviates from the straight path and moves through the tetrahedral site.

DOI: 10.1021/acs.chemmater.5b04862
Chem. Mater. XXXX, XXX, XXX−XXX

First-principles nudged elastic band (NEB) calculations[39] were performed for both the single-vacancy dumbbell as well as the single-vacancy tetrahedral migration corresponding to paths (i) - (iv) (see Figure 2). For (i) - (iii), the single-vacancy dumbbell trajectory resulted in the lower energy as compared to the tetrahedral route. Interestingly, when attempting to calculate the oxygen dumbbell migration for path (iv) we found that it spontaneously relaxed to the tetrahedral site, indicating that the mixed face-sharing Li/Mn environment renders the oxygen saddle point dynamically unstable with respect to the tetrahedral site. Thus, for paths (i) - (iii) the lowest energy single-vacancy correspond to the oxygen dumbbell trajectory whereas path (iv) exhibits the lowest energy for the tetrahedral route. Paths (i)−(iii) resulted in kinetically resolved[40] migration energy barriers (E_a^k) corresponding to (i) 0.78 eV, (ii) 0.60 eV, and (iii) 0.80 eV, respectively. The difference in energy between these barriers is reasonable considering the local cation landscape, as path (ii) face shares with exclusively Li-containing octahedra which reduces the Li-cation repulsion during the migration. Path (iv) was found to exhibit a Li activation barrier 0.56 eV which, while just barely below that of path (ii), was identified as the lowest *single-vacancy* intralayer migration energy.

Next, we examine the effect of neighboring Li vacancy clusters, which has been found to significantly reduce the Li activation energy barrier in layered compounds such as $LiCoO_2$ and $LiTiS_2$.[34,35,41] Here, the lowest energy migration path, e.g., path (iv) from the single-vacancy investigation, was selected for a representative vacancy cluster examination.

Local vacancy clusters usually render the tetrahedral site migration favorable and has been found to "kick in" (e.g., become the dominant diffusion mechanism) for very small deviations from perfect stoichiometry, e.g., $x_{Li} \rightarrow 1$ in Li_xCoO_2.[34,38] In Li_xCoO_2, these vacancy clusters readily form, with no significant vacancy−vacancy repulsion to inhibit fast Li diffusion. In Li_2MnO_3, we find that the divacancy formation energy is 0.054 eV for a single Li-layer divacancy, which is 1 order of magnitude smaller than average Li-ion migration energy barrier in the bulk. Hence, we find no evidence of strong vacancy cluster repulsion which could impact vacancy cluster formation in the Li layer. As an illustration of the effect of neighboring in-plane Li-ion configuration, we observe that in the case of single-vacancy migration, the "gate" Li-ion (marked G in Figure 3a) is displaced 0.35 Å away from its equilibrium position (Figure 3a; gray arrow) during the neighboring Li-ion migration process. The gate Li-ion displacement facilitates the neighboring Li migration and is directly related to the nearest neighbor Li−Li repulsion. Hence, removing a neighboring gate Li, as realized in the divacancy configuration, eliminates the repulsive interaction between the mobile Li-ion and the gate Li-ion and stabilizes the T_{4g}^{Li} site (Figure 3b). The resulting divacancy barrier is approximately 0.37 eV, which is comparable to results found for $LiCoO_2$.[34] The energy scale of the nearest neighbor gate Li−mobile Li interaction is given by the saddle point energy difference between the single- and divacancy migration, e.g., 0.19 eV (Figure 3d; saddle point difference between red circle and blue diamond), which is significant as every 0.05 eV roughly corresponds to an order of magnitude in diffusivity.[42] We can also interpret the energy through a one-dimensional particle coordinate spring motion. The harmonic potential elastic constant for the local Li-ion displacement is thus calculated as 3.22 eV/Å^2, increases the total energy by 0.20 eV/mobile Li corresponding to the 0.35 Å local fluctuation.

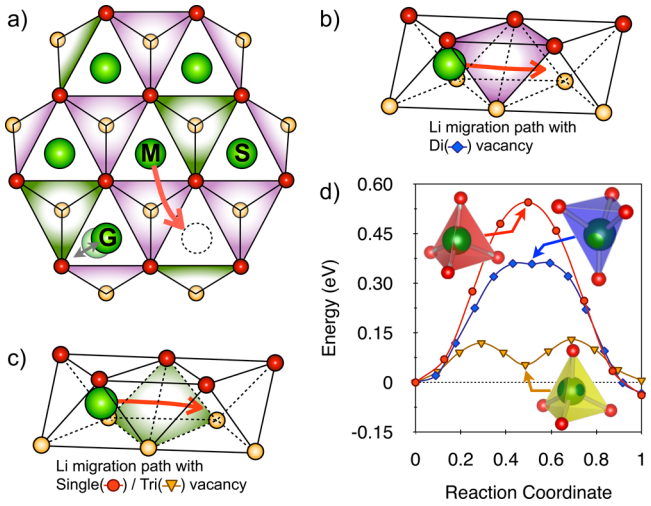

Figure 3. (a) Schematic illustration of the Li-layer with a mobile Li-ion (marked as M) and the gate Li (marked as G). (b) A divacancy mediated Li passing through the T_{4g}^{Li} site and (c) a single- and trivacancy mediated Li passing through the T_{2b}^{Li} site. (d) The Li migration energy as a function of neighboring single-, di-, and trivacancy clusters.

Introducing Li trivacancy clusters on the G- and S-sites, respectively (see Figure 3a) does not significantly further affect the stability of the T_{4g}^{Li} site. Instead, the third vacancy stabilizes the T_{2b}^{Li} site (yellow tetrahedron in Figure 3d), which now becomes the favorable Li-ion migration activated site in a trivacancy clusters local environment (Figure 3c).

In summary, intralayer Li-ion migration in Li_2MnO_3 at high Li content occurs through divacancy and trivacancy cluster mechanisms which enables facile and even fast Li diffusion, similar to best-performing $LiCoO_2$. Hence, while the mobile Li in Li excess Li_xMnO_3 ($1 < x < 2$) experiences a more diverse local cation environments during its migration, the calculated barriers as a function of local vacancy clusters indicate that intralayer Li diffusion in pristine Li_2MnO_3 follows a very similar pattern as previously investigated layered Li intercalation materials (e.g., $LiCoO_2$).

Interlayer Li-Ion Migration. We now turn to interlayer Li migration, which provides a 3D migration mechanism and sets Li_2MnO_3 and other Li-excess materials apart from previously examined layered Li intercalation cathodes. Two options are available for Li migration from the TM-layer to the Li-layer (see Figure 4a). Figure 4 illustrates the neighboring tetrahedral sites between two adjacent octahedral sites in the TM-layer (cyan tetrahedron) as well as the Li-layer (green tetrahedron) and the associated Li migration path.

Not surprisingly we found that attempting to migrate Li through any of the TM tetrahedral sites (T_{2c}^{TM} and T_{4h}^{TM})

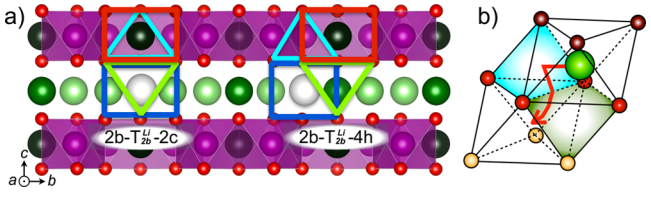

Figure 4. Illustration of the possible migration paths for interlayer (TM to Li layer) Li migration. Cyan indicates the T_{2c}^{TM} and T_{4h}^{TM} TM tetrahedral sites and green the Li-layer T_{2b}^{Li} site.

DOI: 10.1021/acs.chemmater.5b04862
Chem. Mater. XXXX, XXX, XXX−XXX

spontaneously relaxed the Li-ion to the Li-layer tetrahedral sites (T^{Li}_{4g} and T^{Li}_{2b}), as indicated by the red arrow in Figure 4b. Since the T^{Li}_{4g} sites face-share with Mn, the T^{Li}_{2b} site, which can face-share with Li, provides the more favorable intermittent site option for interlayer Li-ion migration. Figure 5a shows the single-vacancy Li-ion migration process as the mobile Li-ion (marked as M) pass through the T^{Li}_{2b} site and thereafter move into the octahedral site.

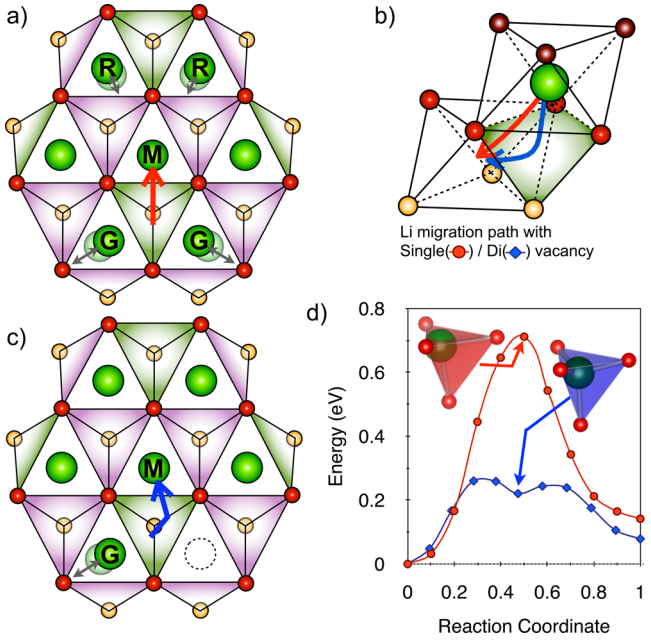

Figure 5. Effects of vacancy clusters on interlayer Li migration. Four neighboring Li-ions are monitored and denoted "G" for gate and "R" for rear. (a) In single-vacancy migration the two gate Li-ions (G) move 0.31 Å and two rear Li-ions (R) move 0.12 Å. (b) Illustration of the mobile Li-ion (M) passing through the oxygen dumbbell path (red arrow) for the single-vacancy and the tetrahedral path (blue arrow) for the divacancy mechanism. (c) In the divacancy mechanism, where one gate Li-ion is removed, the other gate Li-ion move 0.39 Å. (d) The calculated single-vacancy (red) and divacancy (blue) energy profiles as a function of the Li migration path coordinates.

The activation barrier (E^K_a) for this single-vacancy TM-Li layer migration corresponds to approximately 0.64 eV for the 2b-T^{Li}_{2b}-2c (see Figure 5d) and 0.65 eV for the 2b-T^{Li}_{2b}-4h migration path, respectively. While very close in energy, to further investigate the interlayer Li migration, we select the lowest migration energy path, (2b-T^{Li}_{2b}-2c), as a representative interlayer Li migration. Figure 5a illustrates that significant Li−Li interaction is experienced from the neighboring Li-ions in the Li-layer as four out of six first neighboring Li-ions fluctuate from their equilibrium sites during the mobile Li (denoted "M") migration (Figure 5a, gray arrows). Interestingly, we find that the two gate (G) Li-ions move 0.31 Å and two rear (R) Li-ions move 0.12 Å. Hence, we would expect the gate Li-ion vacancies to influence the migration barrier the most. Indeed, removing one of the gate Li-ions (cf. Figure 5b) significantly decreases the Li activation barrier from 0.64 to 0.18 eV (Figure 5d; saddle point difference between red circle and blue diamond). From Figure 5d we also observe that the tetrahedral site T^{Li}_{2b} has evolved from a saddle point to a metastable site (blue arrow in Figure 5b). During the divacancy Li-ion migration, the remaining gate Li-ion is now displaced 0.39 Å (gray arrow in Figure 5c). We emphasize that the divacancy mechanism has a 142% larger effect on the interlayer Li migration as compared with the intralayer migration. In a trivacancy configuration, the tetrahedral site is surrounded by Li vacancies, located at both gate sites in Figure 5a as well as the 2c site in Li-layer. In this case, we find that the trivacancy tetrahedral site is not be able to form a metastable site nor a saddle point. Instead, once slightly perturbed, the TM-layer Li-ion spontaneously migrate (no barrier) into the Li-layer. Hence we surmise that once there are enough Li vacancies in the Li-layer, the TM-layer Li will immediately equilibrate to the Li-layer.

To summarize, we find that interlayer Li migration is also strongly influenced by Li vacancies in the Li-layer. A very low divacancy tetrahedral path barrier of approximately 0.18 eV is found for bulk pristine Li_2MnO_3 at high Li concentrations and should correspond to very rapid interlayer Li mobility. Interestingly, we surmise that intralayer diffusion, while facile, is predicted to be slower than the interlayer counterpart, assuming that the divacancy mechanism is enabled (e.g., enough Li-ion vacancies in the Li-layer). A summary of the Li-ion migration energy barriers of intra- as well as interlayer migration as a function of vacancy clusters is presented in Table 1.

Table 1. Saddle Point Energies (Kinetically Resolved Activation Energy Barrier, E^{K40}_a) as a Function of the Vacancy Cluster Type for Both Intra- and Interlayer Li Migration

	E^K_a (eV)	
defects	intralayer	interlayer
V_{Single}	0.56 (Figure 3)	0.64 (Figure 5)
V_{Di}	0.38 (Figure 3)	0.18 (Figure 5)
V_{Tri}	0.05 (Figure 3)	
Mn def. V_{Single}	0.56 (Figure 7a)	0.80 (Figure 7b)
Mn def. V_{Di}	−0.29 (Figure 7a)	0.70 (Figure 7b)

Li Mobility Dependence on Lattice and Concentration. Previous studies, particularly in layered materials, have shown that not only vacancy clusters but also the lattice change that follows a change in Li concentration[35,38] strongly influences Li diffusivity. In both $LiCoO_2$ and $LiTiS_2$, the vacancy cluster mechanisms initially boost Li diffusion but at lower Li concentrations, the decrease in layer slab space contracts the volume of the activated tetrahedral site, thus inhibiting the Li mobility. In Li_xCoO_2 the layer distance is gradually decreased as a function of Li concentration. However, we do not observe such a strong monotonic behavior in layered Li_2MnO_3, at least for moderate delithiations ($1 < x < 2$). Figure 6a shows the Li_xMnO_3 lattice constant in the c-direction which exhibits an initial rise and then a faint decline as a function of Li concentration for $1 < x < 2$. At $x = 1$, an ordered phase is predicted for Li_xMnO_3 which is usually associated with a sharp dip in Li diffusivity as the Li "lock into" their ordered state. While a complete kinetic exploration of the diffusivity in Li_2MnO_3 as a function of concentration is beyond the scope of this paper, we examined the Li intralayer Li activation barriers close to the ordering concentration of $x = 1$. At this concentration, from thermodynamic considerations (see above) no Li should remain in the TM-layer and the Li-ions are exclusively located at the 4h sites (see Figure 1c, bottom). We constructed a cell with a Li concentration of $x = 0.969$ and

DOI: 10.1021/acs.chemmater.5b04862
Chem. Mater. XXXX, XXX, XXX−XXX

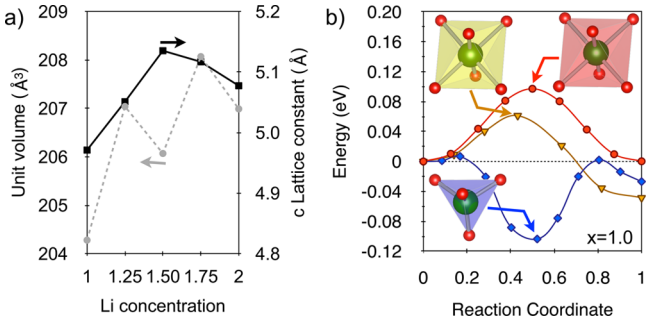

Figure 6. (a) The Li_xMnO_3 lattice constant in the c direction (black squares) and volume (gray circles) of the conventional unit cell for $1 < x < 2$. (b) Representative Li-ion migration barriers for low Li-concentration ($x = 0.969$), where each color follows the same notation as in Figure 3. The vacancies are chosen from the nearest neighbor 4h sites, and the 2c sites are unoccupied as illustrated in Figure 1c, bottom.

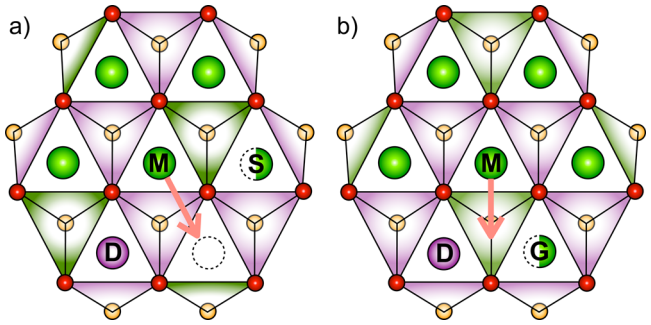

Figure 7. Schematic illustration of Li-ion migration in close interaction with a Mn defect for intralayer (a) and interlayer (b) migration.

introduced di- as well as trivacancies among the nearest neighbor occupied 4h Li sites, where the vacancy positions correspond to the second neighboring octahedral sites in high Li concentration. The Li-ion activation barriers for the single-, di-, and trivacancy clusters are shown in Figure 6b. Interestingly, we find extremely low barriers, even for the single-vacancy mechanism. Furthermore, for the di- and trivacancy clusters, the activated tetrahedral site becomes stable indicating that once a local increase in vacancies is achieved, the Li mobility is highly facile.

Li-Ion Mobility Surrounding a Li-Layer Mn Defect. It has now been firmly established, through both experimental[31,43] as well as theoretical modeling[24] that Li_xMnO_3 is rendered highly unstable against oxygen loss as well as Mn migration into the Li-layer, once the Li concentration drops below $x = 1$, even locally.[24,25] Because of limited oxygen mobility in the bulk material,[24] oxygen deficiency is likely to be limited to the surface region of the particles. However, the Mn migration and subsequent structural rearrangement toward "spinel-like" nuclei is predicted to be feasible in the bulk. Both of these effects are highly probable to impact Li mobility; oxygen loss through a densification of the surface region and Mn defects through a change of the bulk cation landscape and structure. Here we examine the impact on bulk interlayer as well as intralayer Li migration by constructing a model stoichiometric material with a low Mn defect concentration in the Li-layer, e.g., a material where a few Mn have moved from the Mn-layer into the Li-layer, leaving TM layer Mn vacancies behind. Dilute Mn defects are not anticipated to significantly change the charge mechanism or the charge distribution which is supported by the calculated magnetic moments and Bader charges for representative configurations, see the Supporting Information. Nevertheless, we focus on the low Mn defect concentration regime as high Mn defect formation is known to lead to severe structural deformations[13,24] rendering the layered model irrelevant.

We incorporate a Mn defect at a gate Li-ion position (see the purple ion marked "D" in Figure 7) in Li_xMnO_3. Figure 7 also illustrates the mobile Li (marked "M") migration paths close to the Mn defect. The neighboring half-filled Li sites which enable the single-vacancy and divacancy migration mechanisms are denoted "S" (Figure 7a) for side Li-ion and "G" (Figure 7b) for gate Li-ion. We calculated both the oxygen dumbbell and tetrahedral site (T^{Li}_{2b} and T^{Li}_{4g}) migration cases, for both single- and divacancy intralayer scenarios. In all cases, the mobile Li relaxed into the bottom tetrahedral site T^{Li}_{2b} during the NEB calculation. The resulting (lowest) Li-ion migration energy barriers close to a Mn defect are summarized in Table 1.

We find that a Mn defect does not significantly influence intralayer Li-ion migration in the single-vacancy configuration. This is intuitive as, similar to the nondefect case, the mobile Li-ion passes through the T^{Li}_{2b} site (Figure 3c and red tetrahedron in Figure 3d) and hence interacts locally only with neighboring Li cations. On the other hand, in the divacancy configuration, where the "S" position Li-ion is removed, the Mn defect significantly affects the local Li site preference as well as the migration paths, which is similar to the trivacancy migration for the nondefect case (yellow tetrahedron in Figure 3d). For divacancies, neighboring a Mn defect, the T^{Li}_{2b} site is stabilized compared to the neighboring (original) octahedral Li sites. This makes intuitive sense as the Mn defect induces a local spinel nuclei environment and the Li is pushed into the tetrahedral site. For consistency with the other reported barriers, the divacancy intralayer Li activation barrier is presented in Table 1 from the octahedral to the tetrahedral sites, corresponding to a negative energy (−0.29 eV).

Interestingly, we also found a pronounced effect of the Mn defect on the interlayer Li migration. The Li migration energy barriers increased significantly in the presence of a local Mn defect for both the single- and divacancy environments. Specifically, for the single-vacancy configuration the barrier increases to 0.80 eV (from 0.64 eV) and 0.70 eV (from 0.18 eV) for the divacancy. In summary, we expect that even a low concentration of Mn defects in the Li layer will severely impede interlayer Li mobility.

DISCUSSION AND CONCLUSION

We have mapped out the local activation barriers for both intra- as well as interlayer Li migration in Li_xMnO_3 as a function of the diverse local cation environment, and vacancy concentration. We focused on the high Li content regime ($1 < x < 2$) as previous work predict that Li_xMnO_3 delithiates at high Li concentrations through solid solution or weak two-phase behavior. Furthermore, in the high Li content regime, bulk Li_xMnO_3 is thermodynamically stable against Mn migration and oxygen loss,[24] which is likely to change the material both chemically as well as structurally.

Interestingly, we find that Li_xMnO_3, $1 < x < 2$ exhibits facile Li migration barriers. For intralayer migration, the divacancy and trivacancy mechanisms enable Li kinetic barriers in the range of 0.05−0.38 eV which is very similar to the results of $LiCoO_2$. Hence, Li mobility within the alkali layer of Li_xMnO_3

DOI: 10.1021/acs.chemmater.5b04862
Chem. Mater. XXXX, XXX, XXX−XXX

is predicted to be as fast as for $LiCoO_2$,[38,44,45] as long as the original Li_xMnO_3 structure and cation arrangement stays intact. For interlayer Li migration, which generally differentiates the family of Li-excess materials from the stoichiometric layered materials, the divacancy mechanism (two vacancies neighboring the tetrahedral site in the Li-layer) significantly reduces the Li activation barrier from 0.64 to 0.18 eV. A trivacancy causes spontaneous Li migration (no barrier) from the TM-layer to the Li-layer via the stabilized tetrahedral site. This is similar to the case of $LiMn_{0.5}Ni_{0.5}O_2$ where a stabilization of the Li layer tetrahedral site was observed at very low Li concentrations as a function of both TM as well as Li-layer local Li vacancies enabled by an inherent Li^+-Ni^{2+} site exchange in the as-made material.[46]

From these calculations, a fairly clear picture emerges of the delithiation process in Li_xMnO_3 for $1 < x < 2$. The divacancy intralayer Li migration is enabled for very small deviations from stoichiometric Li_xMnO_3 and hence we expect, from both thermodynamic as well as kinetic considerations, some Li to vacate the Li-layer first. However, in concert, as soon as divacancies are formed in the Li-layer, some of the Li in the TM-layer will migrate into the Li-layer as the interlayer divacancy Li migration is faster than the intralayer migration (due to smaller activation barriers). Hence, Li will be removed from the TM-layer as soon as they can be accommodated in the Li-layer. This process is also supported by the thermodynamic prediction of the Li extraction.[24] In summary, we conclude that the low barriers, for both in-layer as well as between-layer migration, resulting from the vacancy cluster mechanisms enable highly mobile Li in structurally and chemically intact bulk Li_xMnO_3.

In contrast, all available experiments show Li_xMnO_3 as having high impedance, low rate, and slow Li diffusion.[21,28,29,31] To resolve this apparent discrepancy, we suggest that the experimentally observed low rate performance of Li_xMnO_3 and related materials is not due to inherently slow bulk Li diffusion but instead to surface reconstruction/densification due to first-cycle oxygen loss[43,47] and emerging Mn defects in the Li-layer with its associated structural changes.[28] This is indirectly supported by recent work by Croy et al.[48] showing that carbon pretreatment of micronsized Li_2MnO_3 significantly improves its performance. Carbon pretreatment will impact the electronic and possible ionic conductivity of the particle surface and particle−particle transport but cannot affect the bulk ionic or electronic conductivity of macroscopic particles.

It is important to note that Mn migration into the Li-layer is predicted to occur if Li is removed beyond $x < 1$ even locally, e.g., for inhomogeneous Li extraction.[49] To examine the impact of Mn migration on the Li mobility, we calculated the intra- and interlayer Li migration barriers surrounding a Mn defect in the Li-layer. We found that the defect causes a local site crossover, where Li now prefers the neighboring tetrahedral site as compared to the original octahedral site. While the investigated migration barriers remain reasonable, the structural effect of the spinel nuclei is likely to negatively impact interlayer Li migration. Furthermore, the Li mobility from the TM-layer to the Li-layer is notably increased (from 0.18 to 0.7 eV for the divacancy mechanism) indicating that the extra capacity available in the TM-layer will be much more sluggish to access and may be eventually "locked out" as a function of increasing Mn defect formations in the Li layer. Finally, we emphasize that reconstruction/densification of the surface will globally affect Li mobility into/from the particles and that the introduction of interfaces within the material, grain boundaries, etc. associated with a composite microstructure are not considered in this work.

In conclusion, our work strongly indicates that Li_xMnO_3, as an end-member "worst-case" representative of the layered Li-excess materials, does not inherently exhibit inferior Li mobility. Instead we suggest that there may be changes to the surface (oxygen loss/densification) and bulk chemistry (Mn migration) that degrades the pristine material when exposed to an electrochemical environment. Our results encourage further work in surface characterization of the Li excess materials, as a function of morphology to elucidate if surface oxygen loss and subsequent reconstruction can be correlated to the inferior rate performance is important family of the materials and possibly mitigated.

Computational Methods. The total energy results as well as the Li mobility barriers were calculated using Density Functional Theory (DFT) which is utilized by Vienna *ab inito* Simulation Package (VASP)[50−53] with the projector augmented wave (PAW)[54,55] pseudopotential method. The exchange correlation functional is chosen as the generalized gradient approximation (GGA+U)[56−58] with an on-site Hubbard parameter (U_{Mn} = 4.5 eV[59]). A supercell size of 4 × 4 × 2 was used to investigate all Li-migrations which contains 32 f.u. (192 atoms). The calculations were converged within 1 meV, enabled by a cutoff energy of 520 eV, and k-point sampling density of 1000 (k-point/reciprocal cell), adjusted by the size of the supercell.

■ ASSOCIATED CONTENT

Supporting Information

The Supporting Information is available free of charge on the ACS Publications website at DOI: 10.1021/acs.chemmater.5b04862.

Magnetic moments and calculated Bader charges for some representative configurations (PDF)

■ AUTHOR INFORMATION

Corresponding Author

*E-mail: kapersson@lbl.gov. Phone: +1 (510) 486-7218.

Notes

The authors declare no competing financial interest.

■ ACKNOWLEDGMENTS

This work intellectually led by the Battery Materials Research (BMR) program, under the Assistant Secretary for Energy Efficiency and Renewable Energy, Office of Vehicle Technologies of the U.S. Department of Energy, Contract No. DE-AC02-05CH11231. Dr. Ding was supported as part of the Center for the Next Generation of Materials by Design, an Energy Frontier Research Center funded by the U.S. Department of Energy, Office of Science, Basic Energy Sciences under Contract No. DE-AC36-08GO28308 to NREL. Finally, this research used resources of the National Energy Research Scientific Computing Center (NERSC).

■ REFERENCES

(1) Wang, Y.; Wang, J.; Yang, J.; Nuli, Y. High-Rate LiFePO4 Electrode Material Synthesized by a Novel Route from $FePO_4 \cdot 4H_2O$. *Adv. Funct. Mater.* **2006**, *16*, 2135−2140.

DOI: 10.1021/acs.chemmater.5b04862
Chem. Mater. XXXX, XXX, XXX−XXX

(2) Huang, Y.-H.; Goodenough, J. B. High-Rate $LiFePO_4$ Lithium Rechargeable Battery Promoted by Electrochemically Active Polymers. *Chem. Mater.* **2008**, *20*, 7237−7241.
(3) Buqa, H.; Goers, D.; Holzapfel, M.; Spahr, M. E.; Novák, P. High Rate Capability of Graphite Negative Electrodes for Lithium-Ion Batteries. *J. Electrochem. Soc.* **2005**, *152*, A474−8.
(4) Kamaya, N.; Homma, K.; Yamakawa, Y.; Hirayama, M.; Kanno, R.; Yonemura, M.; Kamiyama, T.; Kato, Y.; Hama, S.; Kawamoto, K.; Mitsui, A. A lithium superionic conductor. *Nat. Mater.* **2011**, *10*, 682−686.
(5) Mo, Y.; Ong, S. P.; Ceder, G. First Principles Study of the $Li_{10}GeP_2S_{12}$ Lithium Super Ionic Conductor Material. *Chem. Mater.* **2012**, *24*, 15−17.
(6) Thackeray, M. M. Manganese oxides for lithium batteries. *Prog. Solid State Chem.* **1997**, *25*, 1−71.
(7) Lu, Z.; MacNeil, D. D.; Dahn, J. R. Layered Cathode Materials $Li[Ni_xLi_{1/3-2x/3)}Mn_{(2/3-x/3}]O_2$ for Lithium-Ion Batteries. *Electrochem. Solid-State Lett.* **2001**, *4*, A191−4.
(8) Kalyani, P.; Chitra, S.; Mohan, T.; Gopukumar, S. Lithium metal rechargeable cells using Li_2MnO_3 as the positive electrode. *J. Power Sources* **1999**, *80*, 103−106.
(9) Robertson, A. D.; Bruce, P. G. Mechanism of Electrochemical Activity in Li_2MnO_3. *Chem. Mater.* **2003**, *15*, 1984−1992.
(10) Thackeray, M. M.; Johnson, C. S.; Vaughey, J. T.; Li, N.; Hackney, S. A. Advances in manganese-oxide 'composite' electrodes for lithium-ion batteries. *J. Mater. Chem.* **2005**, *15*, 2257−2267.
(11) Rana, J.; Stan, M.; Kloepsch, R.; Li, J.; Schumacher, G.; Welter, E.; Zizak, I.; Banhart, J.; Winter, M. Structural Changes in Li_2MnO_3 Cathode Material for Li-Ion Batteries. *Adv. Energy Mater.* **2014**, *4*, 1300998.
(12) Lim, J.-M.; Kim, D.; Lim, Y.-G.; Park, M.-S.; Kim, Y.-J.; Cho, M.; Cho, K. The origins and mechanism of phase transformation in bulk Li_2MnO_3: first-principles calculations and experimental studies. *J. Mater. Chem. A* **2015**, *3*, 7066−7076.
(13) Croy, J. R.; Iddir, H.; Gallagher, K.; Johnson, C. S.; Benedek, R.; Balasubramanian, M. First-charge instabilities of layered-layered lithium-ion-battery materials. *Phys. Chem. Chem. Phys.* **2015**, *17*, 24382−24391.
(14) Manthiram, A. Materials Challenges and Opportunities of Lithium Ion Batteries. *J. Phys. Chem. Lett.* **2011**, *2*, 176−184.
(15) Xu, B.; Fell, C. R.; Chi, M.; Meng, Y. S. Identifying surface structural changes in layered Li-excess nickel manganese oxides in high voltage lithium ion batteries: A joint experimental and theoretical study. *Energy Environ. Sci.* **2011**, *4*, 2223−11.
(16) Dong, X.; Xu, Y.; Xiong, L.; Sun, X.; Zhang, Z. Sodium substitution for partial lithium to significantly enhance the cycling stability of Li_2MnO_3 cathode material. *J. Power Sources* **2013**, *243*, 78−87.
(17) Kang, S. H.; Amine, K. Layered $Li(Li_{0.2}Ni_{0.15+0.5z}Co_{0.10}Mn_{0.55-0.5z})O_{2-z}F_z$ cathode materials for Li-ion secondary batteries. *J. Power Sources* **2005**, *146*, 654−657.
(18) Zheng, J.; Wu, X.; Yang, Y. Improved electrochemical performance of $Li[Li_{0.2}Mn_{0.54}Ni_{0.13}Co_{0.13}]O_2$ cathode material by fluorine incorporation. *Electrochim. Acta* **2013**, *105*, 200−208.
(19) Johnson, C. S.; Kim, J.-S.; Lefief, C.; Li, N.; Vaughey, J. T.; Thackeray, M. M. The significance of the Li_2MnO_3 component in 'composite' $xLi_2MnO_3{\cdot}(1\text{-}x)\ LiMn_{0.5}Ni_{0.5}O_2$ electrodes. *Electrochem. Commun.* **2004**, *6*, 1085−1091.
(20) Ellis, B. L.; Lee, K. T.; Nazar, L. F. Positive Electrode Materials for Li-Ion and Li-Batteries. *Chem. Mater.* **2010**, *22*, 691−714.
(21) Marom, R.; Amalraj, S. F.; Leifer, N.; Jacob, D.; Aurbach, D. A review of advanced and practical lithium battery materials. *J. Mater. Chem.* **2011**, *21*, 9938−17.
(22) Johnson, C. S.; Li, N.; Vaughey, J. T.; Hackney, S. A.; Thackeray, M. M. Lithium−manganese oxide electrodes with layered−spinel composite structures $xLi_2MnO_3{\cdot}(1\text{-}x)Li_{1+y}Mn_{2-y}O_4$ ($0 < x < 1$, $0 \le y \le 0.33$) for lithium batteries. *Electrochem. Commun.* **2005**, *7*, 528−536.
(23) Dogan, F.; Croy, J. R.; Balasubramanian, M.; Slater, M. D.; Iddir, H.; Johnson, C. S.; Vaughey, J. T.; Key, B. Solid State NMR Studies of Li_2MnO_3 and Li-Rich Cathode Materials: Proton Insertion, Local Structure, and Voltage Fade. *J. Electrochem. Soc.* **2015**, *162*, A235−A243.
(24) Lee, E.; Persson, K. A. Structural and Chemical Evolution of the Layered Li-Excess Li_xMnO_3 as a Function of Li Content from First-Principles Calculations. *Adv. Energy Mater.* **2014**, *4*, 1400498.
(25) Qian, D.; Xu, B.; Chi, M.; Meng, Y. S. Uncovering the roles of oxygen vacancies in cation migration in lithium excess layered oxides. *Phys. Chem. Chem. Phys.* **2014**, *16*, 14665−14668.
(26) Koga, H.; Croguennec, L.; Menetrier, M.; Mannessiez, P.; Weill, F.; Delmas, C.; Belin, S. Operando X-ray Absorption Study of the Redox Processes Involved upon Cycling of the Li-Rich Layered Oxide $Li_{1.20}Mn_{0.54}Co_{0.13}Ni_{0.13}O_2$ in Li Ion Batteries. *J. Phys. Chem. C* **2014**, *118*, 5700−5709.
(27) Sathiya, M.; Rousse, G.; Ramesha, K.; Laisa, C. P.; Vezin, H.; Sougrati, M. T.; Doublet, M.-L.; Foix, D.; Gonbeau, D.; Walker, W.; Prakash, A. S.; Ben Hassine, M.; Dupont, L.; Tarascon, J.-M. Reversible anionic redox chemistry in high-capacity layered-oxide electrodes. *Nat. Mater.* **2013**, *12*, 827−835.
(28) Li, Y.; Bareno, J.; Bettge, M.; Abraham, D. P. Unexpected Voltage Fade in LMR-NMC Oxides Cycled below the "Activation" Plateau. *J. Electrochem. Soc.* **2015**, *162*, A155−A161.
(29) Dong, X.; Xu, Y.; Yan, S.; Mao, S.; Xiong, L.; Sun, X. Towards low-cost, high energy density Li_2MnO_3 cathode materials. *J. Mater. Chem. A* **2015**, *3*, 670−679.
(30) Yu, H.; Wang, Y.; Asakura, D.; Hosono, E.; Zhang, T.; Zhou, H. Electrochemical kinetics of the $0.5Li_2MnO_3{\cdot}0.5LiMn_{0.42}Ni_{0.42}Co_{0.16}O_2$ 'composite' layered cathode material for lithium-ion batteries. *RSC Adv.* **2012**, *2*, 8797−11.
(31) Yu, H.; Zhou, H. High-Energy Cathode Materials (Li_2MnO_3−$LiMO_2$) for Lithium-Ion Batteries. *J. Phys. Chem. Lett.* **2013**, *4*, 1268−1280.
(32) Chen, Y.-C.; Huo, M.; Liu, Y.; Chen, T.; Leng, C.-C.; Li, Q.; Sun, Z.-L.; Song, L.-J. Structural, Electrical, and Lithium Ion Dynamics of Li_2MnO_3 from Density Functional Theory. *Chin. Phys. Lett.* **2015**, *32*, 017102−5.
(33) Hoang, K. Defect Physics, Delithiation Mechanism, and Electronic and Ionic Conduction in Layered Lithium Manganese Oxide Cathode Materials. *Phys. Rev. Appl.* **2015**, *3*, 024013−17.
(34) Van der Ven, A.; Ceder, G. Lithium diffusion mechanisms in layered intercalation compounds. *J. Power Sources* **2001**, *97−98*, 529−531.
(35) van der Ven, A.; Bhattacharya, J.; Belak, A. A. Understanding Li Diffusion in Li-Intercalation Compounds. *Acc. Chem. Res.* **2013**, *46*, 1216−1225.
(36) Xiao, R.; Li, H.; Chen, L. Density Functional Investigation on Li_2MnO_3. *Chem. Mater.* **2012**, *24*, 4242−4251.
(37) Wang, R.; He, X.; He, L.; Wang, F.; Xiao, R.; Gu, L.; Li, H.; Chen, L. Atomic Structure of Li_2MnO_3 after Partial Delithiation and Re-Lithiation. *Adv. Energy Mater.* **2013**, *3*, 1358−1367.
(38) Van der Ven, A.; Ceder, G. Lithium Diffusion in Layered Li_xCoO_2. *Electrochem. Solid-State Lett.* **1999**, *3*, 301−304.
(39) Jónsson, H.; Mills, G.; Jacobsen, K. W. Nudged elastic band method for finding minimum energy paths of transitions. *Classical and quantum dynamics in condensed phase simulations* **1997**, *1*, 385−404.
(40) Van der Ven, A.; Ceder, G.; Asta, M.; Tepesch, P. D. First-principles theory of ionic diffusion with nondilute carriers. *Phys. Rev. B: Condens. Matter Mater. Phys.* **2001**, *64*, 184307−17.
(41) Urban, A.; Lee, J.; Ceder, G. The Configurational Space of Rocksalt-Type Oxides for High-Capacity Lithium Battery Electrodes. *Adv. Energy Mater.* **2014**, *4*, 1400478.
(42) Mo, Y.; Ong, S. P.; Ceder, G. Insights into Diffusion Mechanisms in P2 Layered Oxide Materials by First-Principles Calculations. *Chem. Mater.* **2014**, *26*, 5208−5214.
(43) Yan, P.; Xiao, L.; Zheng, J.; Zhou, Y.; He, Y.; Zu, X.; Mao, S. X.; Xiao, J.; Gao, F.; Zhang, J.-G.; Wang, C.-M. Probing the Degradation

DOI: 10.1021/acs.chemmater.5b04862
Chem. Mater. XXXX, XXX, XXX−XXX

Mechanism of Li_2MnO_3 Cathode for Li-Ion Batteries. *Chem. Mater.* **2015**, *27*, 975−982.
(44) Morgan, D.; Van der Ven, A.; Ceder, G. Li Conductivity in Li_xMPO_4 (M = Mn,Fe,Co,Ni) Olivine Materials. *Electrochem. Solid-State Lett.* **2004**, *7*, A30−3.
(45) Bhattacharya, J.; van der Ven, A. First-principles study of competing mechanisms of nondilute Li diffusion in spinel Li_xTiS_2. *Phys. Rev. B: Condens. Matter Mater. Phys.* **2011**, *83*, 144302−9.
(46) Bréger, J.; Meng, Y. S.; Hinuma, Y.; Kumar, S.; Kang, K.; Shao-Horn, Y.; Ceder, G.; Grey, C. P. Effect of High Voltage on the Structure and Electrochemistry of $LiNi_{0.5}Mn_{0.5}O_2$: A Joint Experimental and Theoretical Study. *Chem. Mater.* **2006**, *18*, 4768−4781.
(47) Lin, F.; Markus, I. M.; Nordlund, D.; Weng, T.-C.; Asta, M. D.; Xin, H. L.; Doeff, M. M. Surface reconstruction and chemical evolution of stoichiometric layered cathode materials for lithium-ion batteries. *Nat. Commun.* **2014**, *5*, 3529.
(48) Croy, J. R.; Park, J. S.; Dogan, F.; Johnson, C. S.; Key, B.; Balasubramanian, M. First-Cycle Evolution of Local Structure in Electrochemically Activated Li_2MnO_3. *Chem. Mater.* **2014**, *26*, 7091−7098.
(49) Ruther, R. E.; Dixit, H.; Pezeshki, A. M.; Sacci, R. L.; Cooper, V. R.; Nanda, J.; Veith, G. M. Correlating Local Structure with Electrochemical Activity in Li_2MnO_3. *J. Phys. Chem. C* **2015**, *119*, 18022−18029.
(50) Kresse, G.; Hafner, J. *Ab initio* molecular dynamics for liquid metals. *Phys. Rev. B: Condens. Matter Mater. Phys.* **1993**, *47*, 558−561.
(51) Kresse, G.; Hafner, J. *Ab initio* molecular-dynamics simulation of the liquid-metal-amorphous-semiconductor transition in germanium. *Phys. Rev. B: Condens. Matter Mater. Phys.* **1994**, *49*, 14251−14269.
(52) Kresse, G.; Furthmüller, J. Efficiency of ab-initio total energy calculations for metals and semiconductors using a plane-wave basis set. *Comput. Mater. Sci.* **1996**, *6*, 15−50.
(53) Kresse, G.; Furthmüller, J. Efficient iterative schemes for *ab initio* total-energy calculations using a plane-wave basis set. *Phys. Rev. B: Condens. Matter Mater. Phys.* **1996**, *54*, 11169−11186.
(54) Blöchl, P. E. Projector augmented-wave method. *Phys. Rev. B: Condens. Matter Mater. Phys.* **1994**, *50*, 17953−17979.
(55) Kresse, G.; Joubert, D. From ultrasoft pseudopotentials to the projector augmented-wave method. *Phys. Rev. B: Condens. Matter Mater. Phys.* **1999**, *59*, 1758−1775.
(56) Perdew, J. P.; Burke, K.; Ernzerhof, M. Generalized Gradient Approximation Made Simple. *Phys. Rev. Lett.* **1996**, *77*, 3865−3868.
(57) Perdew, J. P.; Burke, K.; Ernzerhof, M. Generalized Gradient Approximation Made Simple. *Phys. Rev. Lett.* **1996**, *77*, 3865; *Phys. Rev. Lett.* **1997**, *78*, 1396−1396.
(58) Liechtenstein, A. I.; Anisimov, V. I.; Zaanen, J. Density-functional theory and strong interactions: Orbital ordering in Mott-Hubbard insulators. *Phys. Rev. B: Condens. Matter Mater. Phys.* **1995**, *52*, R5467−R5470.
(59) Zhou, F.; Cococcioni, M.; Marianetti, C. A.; Morgan, D.; Ceder, G. First-principles prediction of redox potentials in transition-metal compounds with LDA+U. *Phys. Rev. B: Condens. Matter Mater. Phys.* **2004**, *70*, 235121−8.

DOI: 10.1021/acs.chemmater.5b04862
Chem. Mater. XXXX, XXX, XXX−XXX